Journal of Alloys and Compounds 509 (2011) 6725–6730

Contents lists available at ScienceDirect

Journal of Alloys and Compounds

journal homepage: www.elsevier.com/locate/jallcom

Defect mediated photocatalytic activity in shape-controlled ZnO nanostructures

Jagriti Gupta, K.C. Barick[1], D. Bahadur*

Department of Metallurgical Engineering and Materials Science, Indian Institute of Technology Bombay, Mumbai 400076, India

ARTICLE INFO

Article history:
Received 8 January 2011
Received in revised form 26 March 2011
Accepted 28 March 2011
Available online 5 April 2011

Keywords:
Nanostructures
ZnO
Shape-control synthesis
Photocatalysis
Magnetism

ABSTRACT

Shape-controlled ZnO nanostructures were synthesized through a facile soft-chemical approach by varying the concentration of OH^- ions. X-ray diffraction and Raman spectra reveal the formation of highly crystalline single-phase hexagonal wurtzite nanostructure. It has been observed that the concentration of OH^- ions plays an important role in controlling the shape of ZnO nanostructures. TEM micrographs indicate that well-spherical particles of size about 8 nm were formed at lower concentration of OH^- ions whereas the higher concentration of OH^- ions favor the formation of nanorods of length 30–40 nm. The optical studies confirmed that the band gap and near band edge emission of ZnO nanostructures are strongly dependent on the shape of particles. Furthermore, the decrease in the intensity of green emission as shape of particles changes from sphere to rod indicates the suppressing of defect density, which in turn influences the photocatalytic activity and ferromagnetic-like behavior of ZnO nanostructures.

1. Introduction

ZnO nanostructures with a wide bandgap (3.37 eV) and large exciton binding energy (60 meV) at room temperature have been the subject of intense research because of their unique electrical and optical properties [1–4]. Recently, ZnO has been used as an alternative to TiO_2 for photocatalytic degradation of organic contaminants due to its non-toxic and higher photocatalytic efficiency with good sensing behavior [5–7]. ZnO nanostructures with high surface area exhibit higher photocatalytic activity for the degradation of organic pollutants in water than their bulk counterparts. In addition, these ZnO catalyzed reactions can be performed in nearly neutral solution, which is an added advantage of ZnO over its competitors and makes ZnO, a significant candidate for environmental detoxification by photocatalysis. However, an efficient photocatalytic process requires the suppression of electron–hole recombination by trapping of charge carriers at defect states such as oxygen vacancies. Thus, the photocatalytic activity of ZnO can be refrained either by presence of inherent defect states related to shape, size and morphology, or intentionally created defect states within the band gap through doping with transition metal ions [8–11]. Although ZnO structures can be realized in varieties of forms, such as nanoparticles [5,15], nanowires [4], nanorods [12], nanotubes [13], nanohelices [14], nanobelts [3], nanotetrapods [15] and nanoclusters [11], the studies concerning the effect of ZnO shape and size on its photocatalysis are very scarce [16–19]. Chu et al. observed that the photocatalytic behavior of ZnO is strongly dependent on the surface structure [18]. Zheng et al. reported that the photocatalytic activity of ZnO nanocrystals is mainly dependent on the type and concentration of oxygen defects [19]. Furthermore, oxygen defects in ZnO nanostructures have been demonstrated to impart ferromagnetic behavior with a Curie point above room temperature [12,20–23]. Thus, the study of defect induced properties of ZnO nanostructures with controlled shape and size is essential for their potential application in the diverse area of nanotechnology.

Herein, a facile soft-chemical approach is demonstrated for the fabrication of shape-controlled ZnO nanostructures at low-temperature without using any complexing agents such as surfactants or polymers. It has been observed that the morphology of ZnO nanostructures changes from spherical shaped nanoparticles to anisotropic nanorods simply by varying the concentration of OH^- ions. This, we believe, changes the defect density. Hence, we have investigated the defect induced photocatalytic activity of ZnO nanostructures (due to different shapes) along with their magnetic properties as an additional functionality.

2. Materials and methods

Shape-controlled ZnO nanostructures were synthesized by refluxing 50 mM zinc acetate dihydrate in ethanol medium for 6 h at 70–75 °C using different concentrations of NaOH (50 mM, 200 mM and 400 mM) as catalyst. After completion of the reaction, the colloidal solution was cooled down to room temperature. The resulted precipitates were centrifuged and washed several times with Milli Q water. The samples were dried at 80 °C for further characterization and labelled these as S_1, S_2 and S_3 for samples prepared with NaOH concentrations of 50 mM, 200 mM and 400 mM, respectively.

X-ray diffraction (XRD) patterns were recorded on a PANalytical's X'Pert PRO diffractometer with Cu Kα radiation. The crystallite size and lattice strain of different

* Corresponding author. Tel.: +91 22 2576 7632; fax: +91 22 2572 3480.
E-mail address: dhirenb@iitb.ac.in (D. Bahadur).
[1] Presently at Chemistry Division, Bhabha Atomic Research Centre, Mumbai 400085, India.

0925-8388/$ – see front matter © 2011 Elsevier B.V. All rights reserved.
doi:10.1016/j.jallcom.2011.03.157

Table 1
Crystallite size (nm) and lattice strain (%) of different crystallographic orientations of S_1, S_2 and S_3 samples.

Samples	Crystallite size (nm)			Lattice strain (%)		
	(1 0 1)	(0 0 2)	(1 0 0)	(1 0 1)	(0 0 2)	(1 0 0)
S_1	7.0	6.2	7.1	1.7	1.8	1.5
S_2	12.1	20.3	13.1	1.1	0.65	0.87
S_3	14.0	32.0	13.8	1.01	0.46	0.86

crystallographic orientations (1 0 1), (0 0 2) and (1 0 0) were estimated from the X-ray line broadening using Scherrer calculator of X'Pert High Score Plus software:

$$\text{Crystallite size } (D) = \frac{0.89\lambda}{\beta \cos \theta}$$

$$\text{Lattice strain } (\varepsilon) = \frac{\beta}{4 \tan \theta}$$

where λ is the X-ray wavelength used, β the angular line width at half maximum intensity and θ the Bragg's angle [24]. The transmission electron micrographs were taken by FEG TEM (JEOL JEM-2100F). Raman scattering measurements were performed on Lab RAM HR 800 micro-Raman spectroscopy at backscattering geometry using the 519.26 nm line of an Ar^+ laser as an excitation source with a power of 18 meV. The samples were dispersed in ethanol and UV–visible absorption spectra were recorded with an UV–visible spectrophotometer (Cecil, Model No. CE3021) for the determination of band gap. The photoluminescence (PL) spectra of samples were recorded using Hitachi F 2500 fluorescence spectrophotometer. The elemental analyses of samples were carried out using the energy dispersive spectroscopy (EDS) facility of Hitachi S-3400N scanning electron microscope. The magnetic properties of the samples were measured by physical property measurement system (PPMS, Quantum Design).

Methylene blue (MB, a blue cationic thiazine dye) was used as a model dye to evaluate the photocatalytic activity of the ZnO samples (catalyst). In a typical experiment, 24 mg of catalyst was dispersed in 80 ml of 10 ppm MB aqueous solution. The above reaction mixture was first thoroughly mixed with ultrasonic water bath for 15 min and then magnetically stirred for 30 min in dark to obtain a colloidal solution. The photocatalytic experiments were conducted at room temperature under a UV tube light (Philips TUV 25W/G25T8, wave length 365 nm) positioned horizontally above the liquid surface (colloidal solution was magnetically stirred throughout the photocatalytic experiment to ensure the full suspension of particles). The experiments were conducted for 90 min with 2 ml sample aliquots extracted every 10 min and subsequently centrifuged at 1000 rpm for 10 min. The decomposition of MB was monitored by measuring the absorbance of the supernatant at 665 nm using UV–vis spectrophotometer (Cecil, Model No. CE3021) in quartz cuvette with Milli Q water as reference. For comparison, the photodegradation of MB in absence of ZnO under UV light was also performed.

3. Results and discussion

Fig. 1 shows the XRD patterns of S_1, S_2 and S_3 samples. The XRD analysis reveals that samples exhibit single-phase hexagonal wurtzite nanostructure. From XRD patterns, it is clearly observed that OH^- concentration strongly influences the ZnO crystallinity. On increasing the concentration of OH^- ions, the relative intensity of (0 0 2) plane increases which suggests the change in degree of orientation of samples along the *c*-axis (degree of particle anisotropy). The intensity ratio of (1 0 0)/(0 0 2) changes from 0.95 to 0.75 as OH^- ions concentration increases from 50 to 400 mM. This decrease in intensity ratio of (1 0 0)/(0 0 2) indicates the formation of rod oriented along the *c*-axis at higher concentration of OH^- ions [8]. Furthermore, the crystallite size and lattice strain are different for (1 0 1), (0 0 2) and (1 0 0) crystallographic orientations as depicted in Table 1. In general, there is an increase in average crystallite size and decrease in average lattice disorder on increasing the concentration of OH^- ions. Moreover, the estimated crystallite size for the (0 0 2) plane is greater than the one estimated from (1 0 0) to (1 0 1) planes in S_2 and S_3. Thus, the length of the crystal planes along the *c*-axis, i.e. [0 0 2] direction, is greater than the characteristic lengths in other directions for S_2 and S_3. These results, further confirm the formation of rod oriented along *c*-axis at higher concentration of OH^- ions.

Fig. 2 shows the TEM micrographs of (a) S_1, (b) S_2 and (c) S_3 samples, and HRTEM micrographs of (d) S_1 and (e) S_3 samples. It is clearly observed that well spherical particles of average size about 8 nm were formed at lower concentration of OH^- ions (S_1) whereas higher concentration of OH^- ions (S_3) favor the formation of nanorods of length 30–40 nm. However, at intermediate concentration both particles (average size: 15 nm) and nanorods (20–40 nm) are simultaneously formed. The average interfringe distances of ZnO nanoparticle and nanorod were measured to be ~0.25 nm, which could be assigned to the (0 0 0 2) planes of ZnO [23]. Further, HRTEM image of nanorod indicates the growth of ZnO along the [0 0 0 1] direction. From TEM micrographs, it is well established that the concentration of OH^- ions in the reaction solution strongly control the shape and size of ZnO nanostructures. The chemical reactions for the formation of ZnO nanostructures can be formulated as:

$$Zn^{2+} + 2OH^- \rightarrow Zn(OH)_2$$
$$Zn(OH)_2 \rightarrow ZnO + H_2O$$
$$Zn(OH)_2 + 2OH^- \rightarrow [Zn(OH)_4]^{2-}$$
$$[Zn(OH)_4]^{2-} \rightarrow ZnO + H_2O + 2OH^-$$

$Zn(OH)_2$ is unstable and it can either hydrolyze directly to give the nuclei of ZnO or react with OH^- to form the growth unit of $[Zn(OH)_4]^{2-}$, followed by the polymerization of $[Zn(OH)_4]^{2-}$ to form nuclei of ZnO. The higher OH^- concentration favors the formation of more and more $[Zn(OH)_4]^{2-}$ intermediate, which possibly controls the surface morphology of ZnO. The structure of ZnO based on wurtzite can be treated as being made of alternating planes of tetrahedrally coordinated O^{2-} and Zn^{2+} ions stacked along the *c*-axis [25,26]. The ionic nature of the two elements Zn and O results in the formation of charged crystal faces, which increases their surface energy. It is known that (0 0 0 1) crystal surfaces are Zn-ion termi-

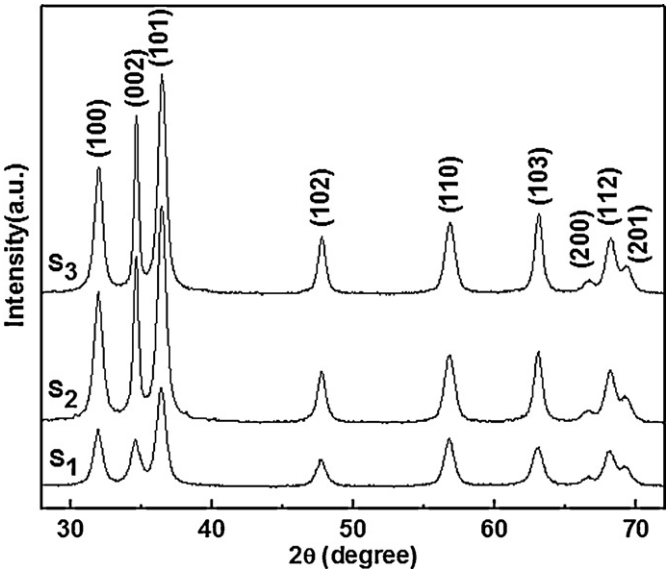

Fig. 1. XRD patterns of S_1, S_2 and S_3 samples.

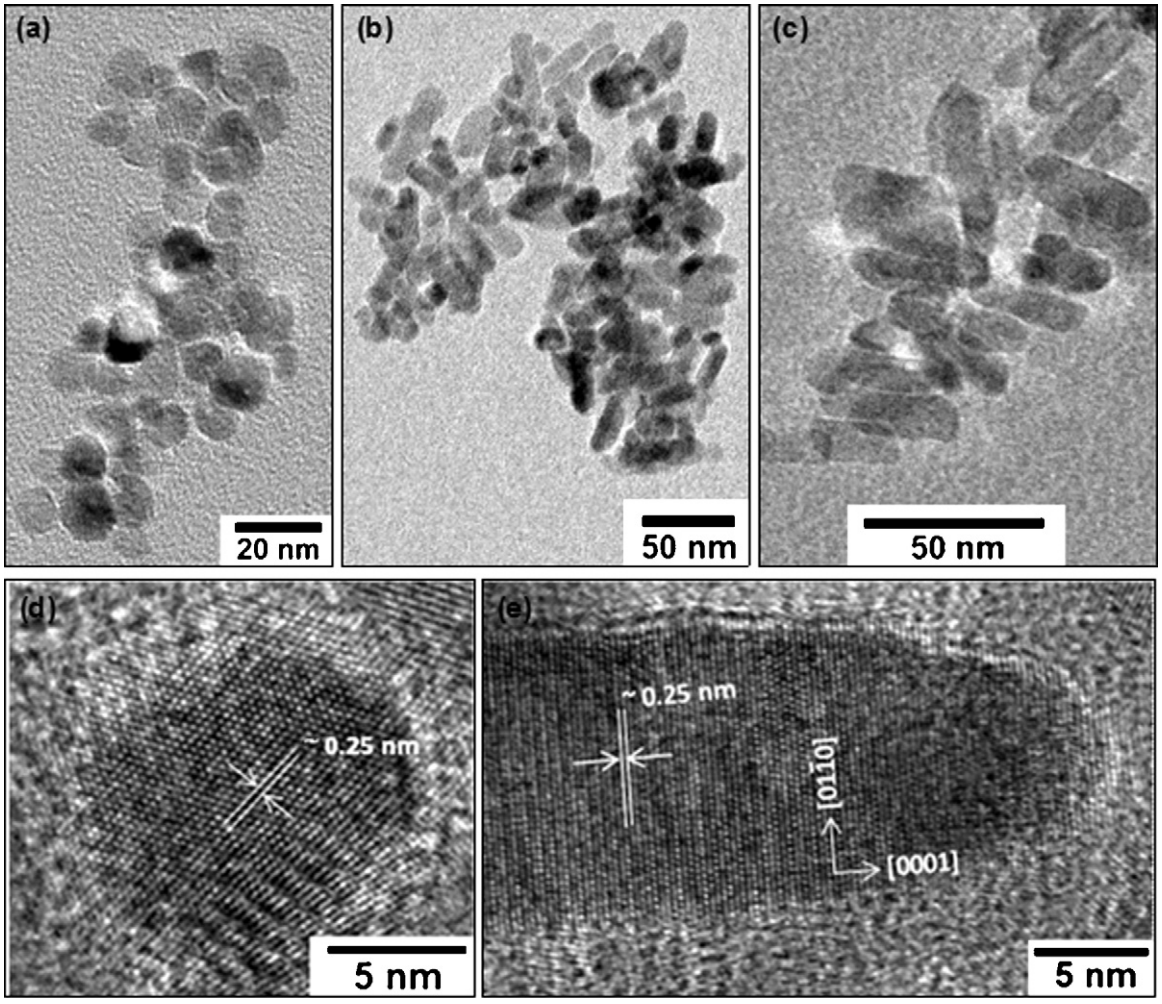

Fig. 2. TEM micrographs of (a) S_1, (b) S_2 and (c) S_3 samples, and HRTEM micrographs of (d) S_1 and (e) S_3 samples.

nated, while the (0 0 0 $\bar{1}$) surfaces are O-ion terminated leading to polarization due to an effective positive and negative charge on these surfaces, respectively. For a crystal growing under kinetic control, the shape and size may be related to the growth rates of the two faces, with the fastest-growing planes disappearing to leave behind the slowest-growing planes as the crystal facets. The schematic representation of possible mechanism for the formation of different shaped ZnO nanostructures is shown in Fig. 3. The negatively charged $[Zn(OH)_4]^{2-}$ intermediate has a strong tendency to bind electrostatically to the most reactive positively charged (0 0 0 1) surface of ZnO nuclei. At higher concentration of OH^- ions (400 mM), growth along (0 0 0 1) surface is almost blocked (reduction of crystal growth along this face as binding of $[Zn(OH)_4]^{2-}$ changes the free energy of the face and thereby reducing its growth) due to the presence of excess $[Zn(OH)_4]^{2-}$ and hence, favors the anisotropic growth along (0 0 0 $\bar{1}$) surface which leads to the formation of nanorods. At low concentration of OH^- ions (50 mM), well-spherical particles were formed due to uniform crystal growth (the concentration of OH^- ions was too low to favor the anisotropic growth). However, at intermediate concentration (200 mM) both uniform as well as anisotropic crystal growth occur leading to the formation of both nanoparticles and nanorods.

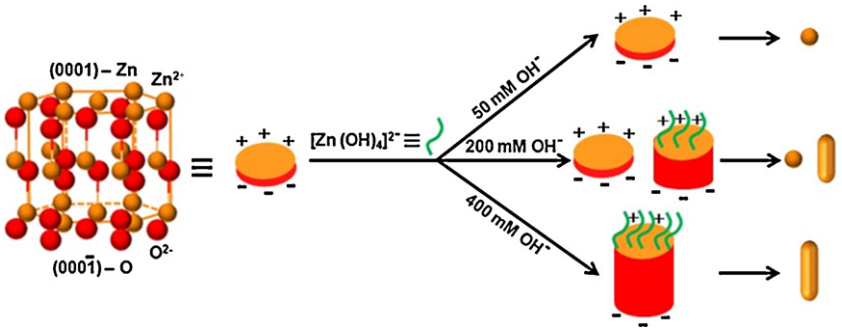

Fig. 3. Schematic representation of possible mechanism for the formation of different shaped ZnO nanostructures.

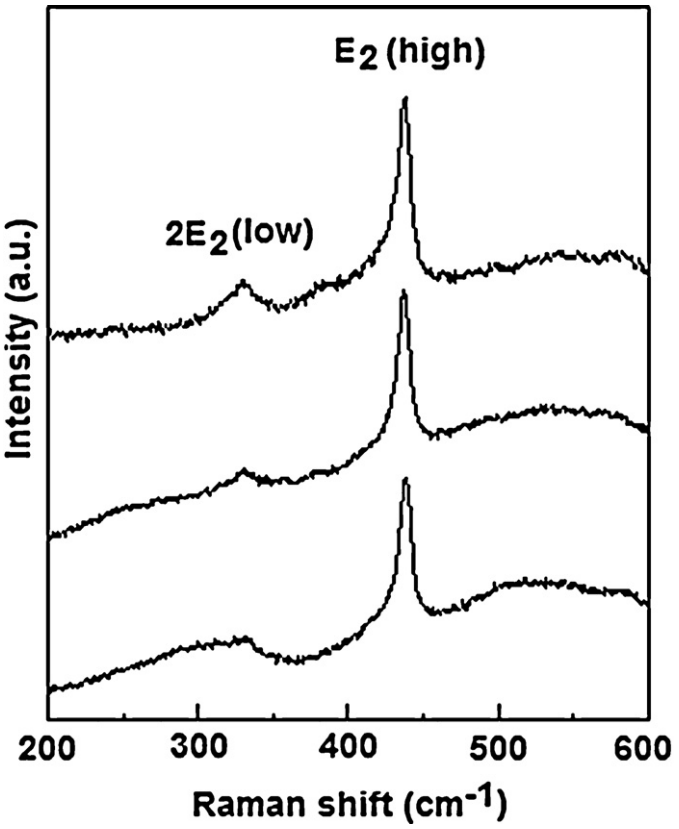

Fig. 4. Room temperature micro-Raman spectra of S_1, S_2 and S_3 samples.

To assess the crystal quality and structural defects, Raman spectroscopic analysis has been carried out on these samples. Fig. 4 shows the room temperature micro-Raman spectra of S_1, S_2 and S_3 samples. In Raman spectra, the predominant peak at 438 cm^{-1} is attributed to the first-order non-polar E_2 (high) phonon mode of ZnO [27]. In addition to the first-order Raman modes, the spectra also show a band at 332 cm^{-1}, which corresponds to the second-order phonon of the low frequency E_2 [27]. The relative intensity of the first order E_2 (high) and second-order E_2 (low) modes of ZnO nanostructures increase on increasing the OH^- ion concentration, which indicates the increase of crystallinity of ZnO nanostructures. The stronger E_2 mode (bending modes of O–O atoms) of S_3 sample indicates its good crystal quality with only a very low level of oxygen vacancy. This result strongly supports the crystallinity behavior of ZnO nanostructures observed in XRD analysis. Furthermore, the micro-Raman spectra confirmed the formation of single-phase hexagonal wurtzite structure.

Fig. 5 shows the UV–visible absorption spectra of S_1, S_2 and S_3 samples. In order to obtain a more precise and quantifiable measure of the band gap energy (E_g), we use the point of inflection, obtained from the minima of first derivative curve of the absorption spectrum [28]. The band gap energy (E_g) thus obtained for S_1, S_2 and S_3 were 3.363, 3.334 and 3.353 eV, respectively. It is observed that the band edge red shifted and broadened as morphology of particles changed from spherical to rod shape. Further, the decrease in band gap energy (E_g) values on increasing the OH^- ions concentration suggests the growth of particles. This trend is in good agreement with the size estimations from XRD and TEM measurements. However, the slight blue shift observed in the absorption edge of our ZnO nanostructures compared to that of bulk (3.3 eV) is possibly due to the quantum confinement effect [28].

Fig. 6 shows the PL spectra of S_1, S_2 and S_3 samples at room temperature (inset shows the magnified PL spectra of emission band

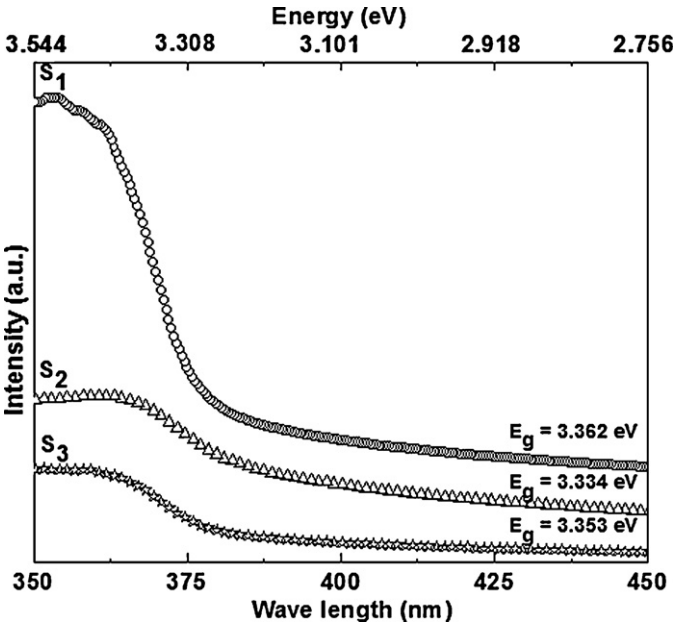

Fig. 5. UV–visible absorption spectra of S_1, S_2 and S_3 samples.

located in the ultraviolet region). To scrutinize the green defect emission (broad band in the visible region), the peaks of the near-band-edge (NBE) emission (sharp band located in the ultraviolet region) in the spectra were normalized to the same value. The NBE emission generally originates from the radiative recombination of excitons, and the green defect emission from the radiative recombination of a photogenerated hole with an electron occupying the singly ionized oxygen vacancy (V_O^+) in ZnO [29,30]. The NBE emission shifts toward the higher wavelength (lower energy) side as seen clearly in the inset of the Fig. 6 as shape of the particles change from spherical to rod, reflecting the change in the exciton energy. The red shift in NBE emission can be attributed to the shape and size of nanostructures [28,31]. Furthermore, the decrease in the intensity of defect emission (I_{Defect}/I_{NBE}) as the shape of particles changes from sphere to rod undoubtedly indicates the suppression of oxygen defect concentration. This is also confirmed by EDS sto-

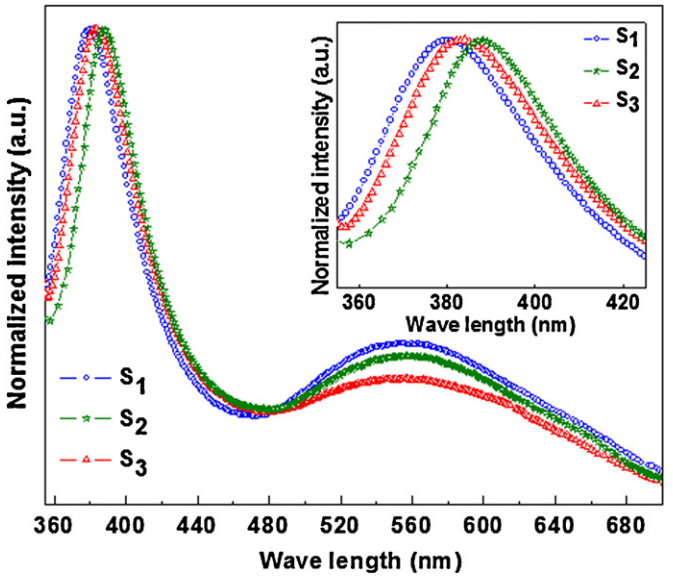

Fig. 6. PL spectra of S_1, S_2 and S_3 samples at room temperature (inset shows the magnified PL spectra of emission band located in the ultraviolet region).

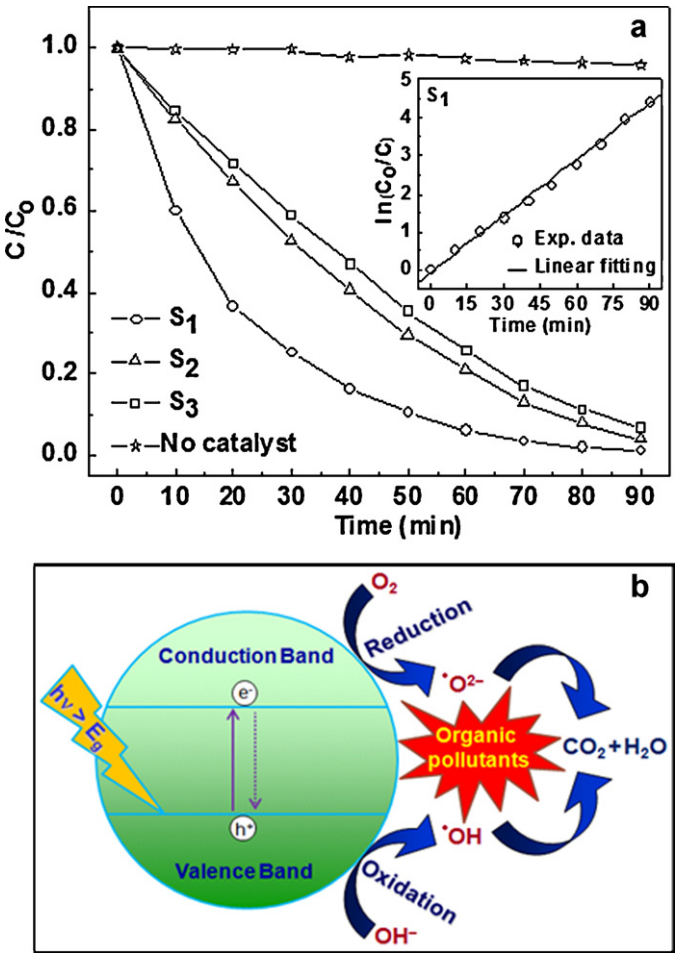

Fig. 7. (a) Photodegradation of methylene blue (MB) under UV irradiation in the presence and absence of photocatalysts (S_1, S_2 and S_3) and (b) the schematic representation of photocatalysis process on ZnO surface (inset of Fig. 7a shows a typical ln (C_o/C) *vs.* time curve of S_1).

ichiometry analysis. Our EDS results revealed an increase of O/Zn atomic ratio (0.48, 0.78, 0.98 for S_1, S_2 and S_3, respectively) in the samples upon change in shape of the particles from sphere to rod. Thus, the present study offers an opportunity to factually reveal the relationship between the defect structure related to shape and luminescence processes.

Fig. 7 shows the (a) photodegradation of methylene blue (MB) under UV irradiation in the presence and absence of catalysts (S_1, S_2 and S_3) and (b) the schematic representation of photocatalysis process on ZnO surface (inset of Fig. 7a shows a typical ln (C_o/C) *vs.* time curve of S_1). In Fig. 7a, C_o and C were the initial concentrations after the equilibrium adsorption of catalyst and the reaction concentration of methylene blue at time t, respectively (in absence of catalyst the feed dye solution represents the true methylene blue concentration at the start of the UV irradiation). The self-degradation of MB without involving photocatalysts was negligible under the UV irradiation whereas the concentration of MB decreased rapidly with exposure time in presence of catalysts, indicating the photocatalytic degradation of the organic dye. It has been observed that the photocatalytic degradation of MB over S_1 is much faster and higher than S_2 and S_3. Furthermore, the photodegradation of the dye over ZnO nanostructures proceeds through a pseudo first order kinetic reaction [11,15], i.e., ln (C_o/C) = kt, where k is the photodegradation rate constant (k = 0.050 min^{-1}, 0.034 min^{-1} and 0.030 min^{-1} for S_1, S_2 and S_3 samples, respectively). The semiconductor photocatalysis (Fig. 7b) is based on the generation of electron (e^-) – hole

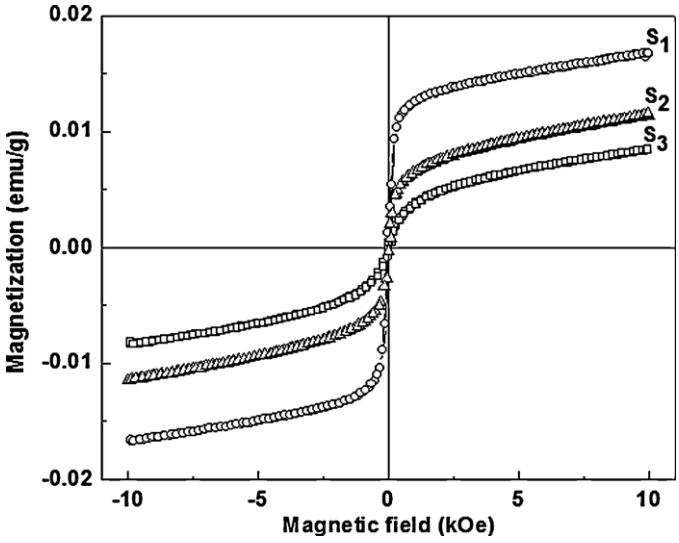

Fig. 8. Room temperature field dependent of magnetization (M *vs.* H) plots of S_1, S_2 and S_3 samples.

(h^+) pair upon UV light irradiation. The electron can be migrated from the valence band to the conduction band, leaving behind hole in the valence band [32]. If the charge separation is maintained, the electron and hole could migrate to the semiconductor surfaces where they participate in redox reactions with the adsorbed organic species [7]. Here, oxygen vacancies work as electron acceptors during the process of photocatalytic reaction and trap the photogenerated electrons temporarily to reduce the surface recombination of electrons and holes. Furthermore, the oxygen vacancies can facilitate the adsorbed O_2 to capture photo-induced electrons, simultaneously producing $^{\bullet}O_2$ radical groups. Thus, we believe that the oxygen vacancies can be considered to be the active sites for controlling the photocatalytic activity of ZnO nanostructures. The higher photocatalytic activity of spherical shape nanosized ZnO can be attributed to the presence of larger amount of oxygen vacancy.

Fig. 8 shows the room temperature field dependent magnetization (M *vs.* H) plots of S_1, S_2 and S_3 samples. The M *vs.* H plots show ferromagnetic like behavior with coercivity of about 20 Oe. Furthermore, the S_1 (nanoparticles) exhibit slightly higher magnetization than that of S_2 (mixture of nanoparticles and nanorods) and S_3 (nanorods). The mechanism responsible for the observed ferromagnetic-like behavior at room temperature is still not clear.

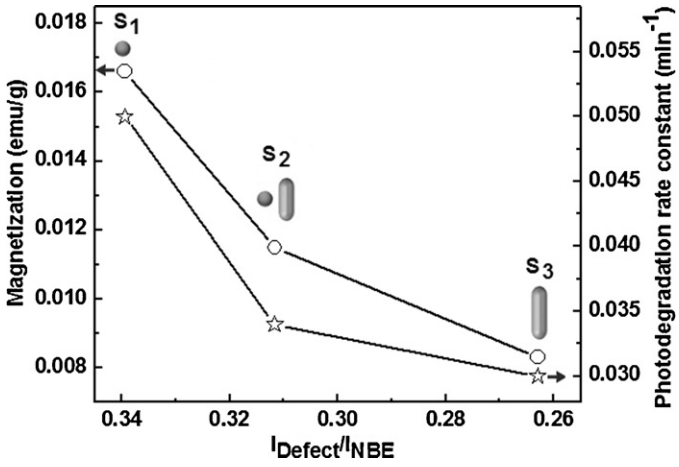

Fig. 9. Correlation of photodegradation and magnetization with concentration of defect.

It was proposed that uncontrolled formation of lattice defects can generate carriers that mediate ferromagnetic behavior [33,34]. It is interesting to note that the rate of photodegradation is maximum for S_1 which is higher than S_2 and S_3 in that order. Similarly magnetization also varies in the same order and it is the defect band in PL spectra. It is tempting to attribute the photodegradation and magnetization to the concentration of defect. The correlation of photodegradation and magnetization with concentration of defect is shown in Fig. 9. Recently, Panigrahy et al. [12] observed a clear relationship between defect-related emissions and the magnetization of ZnO nanorods. Based on the above discussion and previous studies, we believe that the point defects such as oxygen vacancies in the lattice of ZnO nanostructures generate carriers of unquenched magnetic spin moments to mediate ferromagnetic like behavior. These defects are also responsible for photodegradation behavior.

4. Conclusions

We demonstrated a facile soft-chemical approach for the synthesis of shape-controlled ZnO nanostructures by varying the concentration of OH^- ions. The formation of highly crystalline single-phase hexagonal wurtzite nanostructure was evident from XRD and Raman spectra. It was observed that the concentration of OH^- plays an important role in controlling the shape of ZnO nanostructures (either spherical shaped nanoparticles or anisotropic nanorods or mixture of both). The optical, magnetic and photocatalytic properties of ZnO nanostructures are found to be highly dependent on the defect concentration. More specifically, the present investigation suggested that the concentration of defects at the surface of ZnO nanostructures is strongly responsible for the observed ferromagnetic-like ordering and photocatalytic activity.

Acknowledgements

The financial support by Nanomission of DST, Govt. of India is gratefully acknowledged. Jagriti Gupta acknowledges CSIR, India for the award of Junior Research Fellowship (JRF).

References

[1] N. Saito, H. Haneda, T. Sekiguchi, N. Ohashi, I. Sakaguchi, K. Koumoto, Adv. Mater. 14 (2002) 418–421.
[2] V. Bhosle, A. Tiwari, J. Narayan, J. Appl. Phys. 100 (2006) 033713.
[3] B.A. Buchine, W.L. Hughes, F.L. Degertekin, Z.L. Wang, Nano Lett. 6 (2006) 1155–1159.
[4] P.G. Ganesan, K. McGuire, H. Kim, N. Gothard, S. Mohan, A.M. Rao, G. Ramanath, J. Nanosci. Nanotechnol. 5 (2005) 1113–1117.
[5] R.Y. Hong, J.H. Li, L.L. Chen, D.Q. Liu, H.Z. Li, Y. Zheng, J. Ding, Powder Technol. 189 (2009) 426–432.
[6] P.V. Kamat, R. Huehn, R.J. Nicolaescu, J. Phys. Chem. B 106 (2002) 788–794.
[7] N. Daneshvar, D. Salari, A.R. Khataee, J. Photochem. Photobiol. A: Chem. 162 (2004) 317–322.
[8] A. Mclaren, T. Valdes-Solis, G. Li, S.C. Tsang, J. Am. Chem. Soc. 131 (2009) 12540–12541.
[9] J. Wang, P. Liu, X. Fu, Z. Li, W. Han, X. Wang, Langmuir 25 (2009) 1218–1223.
[10] C. Xu, L. Cao, G. Su, W. Liu, X. Qu, Y. Yu, J. Alloys Compd. 497 (2010) 373–376.
[11] K.C. Barick, S. Singh, M. Aslam, D. Bahadur, Micropor. Mesopor. Mater. 134 (2010) 195–202.
[12] B. Panigrahy, M. Aslam, D.S. Misra, M. Ghosh, D. Bahadur, Adv. Funct. Mater. 20 (2010) 1161–1165.
[13] X.P. Shen, A.H. Yuan, Y.M. Hu, Y. Jiang, Z. Xu, Z. Hu, Nanotechnology 16 (2005) 2039–2043.
[14] P.M. Gao, Y. Ding, W.J. Mai, W.L. Hughes, C.S. Lao, Z.L. Wang, Science 309 (2005) 1700–1704.
[15] Q. Wan, T.H. Wang, J.C. Zhao, Appl. Phys. Lett. 87 (1-3) (2005) 083105.
[16] A.C. Dodd, A.J. McKinley, M. Saunders, T. Tsuzuki, J. Nanopart. Res. 8 (2006) 43–51.
[17] D. Li, H. Haneda, Chemosphere 51 (2003) 129–137.
[18] D. Chu, Y. Masuda, T. Ohji, K. Kato, Langmuir 26 (2010) 2811–2815.
[19] Y. Zheng, C. Chen, Y. Zhan, X. Lin, Q. Zheng, K. Wei, J. Zhu, Y. Zhu, Inorg. Chem. 46 (2007) 6675–6682.
[20] A. Sundaresan, R. Bhargavi, N. Rangarajan, U. Siddesh, C.N.R. Rao, Phys. Rev. B 74 (1-4) (2006) 161306.
[21] N.H. Hong, J. Sakai, V. Brizé, J. Phys.: Condens. Matter 19 (1-6) (2007) 036219.
[22] Q. Xu, H. Schmidt, S. Zhou, K. Potzger, M. Helm, H. Hochmuth, M. Lorenz, A. Setzer, P. Esquinazi, C. Meinecke, M. Grundmann, Appl. Phys. Lett. 92 (1-3) (2008) 082508.
[23] K.C. Barick, M. Aslam, V.P. Dravid, D. Bahadur, J. Phys. Chem. C 112 (2008) 15163–15170.
[24] M.S.S. Saravanan, K. Sivaprasad, P. Susila, S.P.K. Babu, Physica B 406 (2011) 165–168.
[25] X. Zhou, Z.-X. Xie, Z.-Y. Jiang, Q. Kuang, S.-H. Zhang, T. Xu, R.-B. Huang, L.-S. Zheng, Chem. Commun. (2005) 5572–5574.
[26] X.Y. Kong, Z.L. Wang, Nano Lett. 3 (2003) 1625–1631.
[27] K.C. Barick, D. Bahadur, J. Nanosci. Nanotechnol. 8 (2008) 4263–4267.
[28] R. Viswanatha, S. Sapra, S.S. Gupta, B. Satpati, P.V. Satyam, B.N. Dev, D.D. Sarma, J. Phys. Chem. B 108 (2004) 6303–6310.
[29] J.J. Wu, H.I. Wen, C.H. Tseng, S.C. Liu, Adv. Funct. Mater. 14 (2004) 806–810.
[30] Y.C. Kong, D.P. Yu, B. Zhang, W. Fang, S.Q. Feng, Appl. Phys. Lett. 78 (1-3) (2001) 407.
[31] Z. Yang, Z. Ye, Z. Xu, B. Zhao, Physica E 42 (2009) 116–119.
[32] Y.H. Zheng, C.Q. Chen, Y.Y. Zhan, X.Y. Lin, Q. Zheng, K.M. Wei, J.F. Zhu, Y.J. Zhu, Inorg. Chem. 46 (2007) 6675–6682.
[33] M. Venkatesan, C.B. Fitzgerald, J.G. Lunney, J.M.D. Coey, Phys. Rev. Lett. 93 (1-4) (2004) 177206.
[34] J.M.D. Coey, M. Venkatesan, C.B. Fitzgerald, Nat. Mater. 4 (2005) 173–179.